




High-resolution spectroscopy and multichannel quantum-defect-theory analysis of the np and nf Rydberg series of Xe below the $^2P_{3/2}$ ionization threshold

H. Herburger,¹ E. N. Toutoudaki ,¹ U. Hollenstein ,¹ and F. Merkt ,^{1,2,3,*}

¹*Institute for Molecular Physical Science, ETH Zürich, 8093 Zürich, Switzerland*

²*Department of Physics, ETH Zürich, 8093 Zürich, Switzerland*

³*Quantum Center, ETH Zürich, 8093 Zürich, Switzerland*



(Received 30 November 2023; accepted 16 February 2024; published 20 March 2024)

This article reports on the application of a long-pulse near-Fourier-transform-limited ultraviolet (UV) laser to a high-precision spectroscopic investigation of the np and nf Rydberg series converging to the $(5p)^5\ ^2P_{3/2}$ ground state of Xe^+ . These series were measured by pulsed-field ionization following single-photon absorption from the $(5p)^5(6s)^1\ ^3P_2$ metastable state of Xe in a doubly skimmed supersonic expansion. They were analyzed by multichannel quantum-defect theory to determine the ionization energies of all natural isotopes of Xe, and to quantify the isotopic shifts of all natural isotopes and the hyperfine structure in the spectra of ^{129}Xe ($I = 1/2$) and ^{131}Xe ($I = 3/2$). Special attention was given to the determination of precise and accurate transition frequencies by careful consideration of systematic uncertainties originating from the DC- and AC-Stark effects, the first- and second-order Doppler effects, the photon-recoil shift, and the calibration of the laser frequency including the analysis of frequency chirps during the laser pulses.

DOI: [10.1103/PhysRevA.109.032816](https://doi.org/10.1103/PhysRevA.109.032816)

I. INTRODUCTION

This article reports on an investigation of high np and nf Rydberg states of Xe by high-resolution spectroscopy from the metastable $(5p)^5(6s)^1\ ^3P_2$ state. The goals of this investigation are to derive from the analysis of these Rydberg series (i) accurate values of the ionization energies of the metastable state of all natural isotopes of Xe and (ii) the hyperfine structure of the $(5p)^5\ ^2P_{3/2}$ ground state of $^{129}\text{Xe}^+$ and $^{131}\text{Xe}^+$ with high accuracy.

The rare-gas atoms (Rg) are, alongside the alkali-metal atoms, the atoms that have been most extensively characterized by high-resolution spectroscopy. The electronic spectrum corresponding to outer-valence-shell excitation is much richer in the rare-gas atoms than in the alkali-metal atoms. Indeed, removal of an electron from the outermost subshell $[(np)^6$ with $n = 2, 3, 4$, and 5 for Rg = Ne, Ar, Kr, and Xe, respectively, and $(ns)^1$ with $n = 2, 3, 4, 5$ and 6 for A = Li, Na, K, Rb, and Cs, respectively] leads to an open-shell $^2P_{J^+}$ ground-state ion core split into two spin-orbit components with $J^+ = 1/2$ and $3/2$ for the rare-gas atoms, but to a closed-shell 1S_0 ground-state ion for the alkali-metal atoms.

Consequently, in the alkali-metal atoms, the Rydberg states form regular series and the ionization energies can be very accurately extrapolated using Rydberg's formula (see, e.g., Refs. [1–5] for recent examples). In the rare-gas atoms, the Rydberg series converge to an open-shell ion-core having a large fine-structure splitting as well as an electric quadrupole and, in the case of nuclei with a nonzero nuclear spin, also (smaller) hyperfine-structure splittings. Singlet and triplet

Rydberg series interact through the spin-orbit interaction and series differing in ℓ by two are coupled through the electrostatic interaction between the Rydberg-electron charge and the ion-core quadrupole moment. As a result, the Rydberg series of the rare-gas atoms are highly perturbed and accurate ionization energies cannot be derived using Rydberg's formula. Neither LS coupling nor jj coupling are suitable to classify the Rydberg states of the rare-gas atoms. Instead, the Racah coupling scheme [6] is used to label the Rydberg series with a $^2P_{J^+}$ ion core as $n\ell^{(l)}[k]_J$, where the presence or absence of the optional l designate series that have an ion core with a dominant $^2P_{1/2}$ and $^2P_{3/2}$ character, respectively, and k and J are the quantum numbers that result from the vector additions $\vec{J}^+ + \vec{\ell}$ and $\vec{k} + \vec{s}$, respectively. Because the spin-orbit and charge-quadrupole interactions involving the Rydberg electron scale with n^{-3} but the spin-orbit and hyperfine interactions in the ion core are n independent, the Rydberg series interact strongly and are difficult to analyze.

For these reasons, the electronic spectrum of the rare-gas atoms has received considerable attention over the years, and extensive data sets are available. In the case of Xe, which is the atom of interest in this article, tables of transition frequencies and term values have been available for a long time [7] and regularly updated. The latest comprehensive update for Xe was made by Sansonetti and Martin in 2005 [8] and the term values they reported are still used in the current version of the NIST atomic data base [1], which also contains references to the original publications. The term values reported in these surveys are given in cm^{-1} with three significant digits after the decimal point, corresponding to an accuracy of about 30 MHz. An extensive list of references has also been provided by Schäfer *et al.* [9] who used the term-value data and data on Rydberg-Rydberg transitions from

*frederic.merkt@phys.chem.ethz.ch

millimeter-wave spectra in a global fit of the energy-level structure of Xe for both the odd-parity (s and d) and even-parity (p and f) Rydberg states using multichannel quantum-defect theory (MQDT).

Three recurrent themes in the studies of the spectrum of Xe are the following. (i) The interactions between series converging on the two spin-orbit components ($^2P_{J^+}$, $J^+ = 3/2, 1/2$) of the ground state of Xe^+ . These interactions lead to rapid autoionization of the series converging on the upper $^2P_{1/2}$ component in the energetic regions between the two ionization thresholds (see, e.g., Refs. [10–15] and the extensive set of references listed by Schäfer *et al.* [9] and Sukhorukov *et al.* [16]). They are elegantly treated by MQDT and several early developments of this collision-theory-based approach to analyze Rydberg spectra were actually prompted by the spectra of the rare-gas atoms, and xenon in particular [10, 17–23]. (ii) The effects of the nuclear spins on the Rydberg series, which exhibit hyperfine splittings that appear, at first sight, to vary randomly from one state to the next, leading to the unsatisfactory situation that sets of hyperfine coupling constants are reported for each individual level of each isotope with nonzero nuclear spin. Recent efforts at a classification of the observed hyperfine structures in the Rydberg states of ^{129}Xe and ^{131}Xe in terms of angular-momentum coupling relations are reported in Refs. [24–26], which contain extensive lists of references on the hyperfine structure in the Rydberg spectra of ^{83}Kr , ^{129}Xe , and ^{131}Xe . MQDT facilitates the interpretation of the hyperfine splittings in Rydberg states of these atoms and relates them exclusively to the hyperfine interaction of the ion-core states ($^2P_{J^+}$, $J^+ = 3/2, 1/2$) [9, 15, 27–30]. Using MQDT, the hyperfine structures observed in Rydberg states are explained through an angular-momentum frame transformation between the short-range and the long-range regions of the electron–ion-core collision system that automatically takes into account the Rydberg-series interactions. (iii) The determination of the ionization energies of the ground $(np)^6\ ^1S_0$ and of the metastable $(np)^5[(n+1)s]^1\ ^3P_2$ states that are often used as initial states when recording transitions to Rydberg levels (see Ref. [16] and references therein) and the corresponding isotopic shifts. Examples of precise determinations of ionization energies from the ground state of Xe can be found in Refs. [29, 31]. A related question concerns the absolute term value (given as $67\,067.547\text{ cm}^{-1}$ in Refs. [1, 8]) of the $(np)^5[(n+1)s]^1\ ^3P_2$ metastable state, which is not easily accessible from the ground state because the transition is a $\Delta J = 2$ transition involving a parity change. A possible way to determine the absolute term value of the metastable state involves the recording of transitions from both states to a common third state. The two $^2P_{J^+}$ ionization thresholds are possible and attractive “third states” in this context. These three themes are at the heart of this article.

We present high-resolution spectra of the np and nf Rydberg states below the $^2P_{3/2}$ ionization threshold of all natural isotopes of Xe recorded following single-photon excitation from the $(np)^5[(n+1)s]^1\ ^3P_2$ metastable state (see Fig. 1 for a schematic energy-level diagram) and their analysis by MQDT. Precise and accurate transition wave numbers are determined using a narrow-band (full width at half maximum of 30 MHz) long-pulse UV laser [32] in combination with a frequency-comb-based calibration procedure relating the

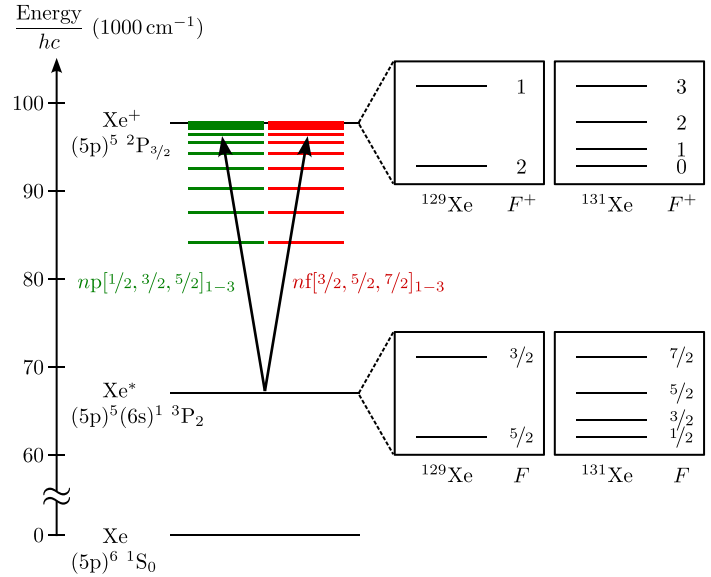


FIG. 1. Schematic energy-level diagram of Xe representing the np and nf Rydberg series converging on the $^2P_{3/2}$ ground state of Xe^+ that are accessible in single-photon transitions (black arrows) from the $(5p)^5(6s)^1\ ^3P_2$ metastable state generated with an electric discharge.

measured frequencies to a GPS-disciplined Rb-atomic-clock standard. These wave numbers are used to determine the ionization energies and their isotopic shifts as well as the hyperfine structure of the ground state of $^{129}\text{Xe}^+$ and $^{131}\text{Xe}^+$ in a least-squares fit based on MQDT calculations using the parameters reported in Ref. [9].

The structure of this article is as follows. Section II summarizes the main features of the experimental procedure and experimental setup. The high-resolution spectra of the np and nf series are presented in Sec. III, which also includes the analysis of statistical and systematic uncertainties of the measured transition frequencies. The MQDT calculations used to determine the ionization energies of the different isotopes and the hyperfine structure of the ground state of $^{129}\text{Xe}^+$ and $^{131}\text{Xe}^+$ are discussed in Sec. IV. Section V summarizes the main findings of this investigation.

II. EXPERIMENTAL SETUP AND PROCEDURE

A schematic overview of the experimental setup is presented in Fig. 2. It consists of a narrow-bandwidth pulsed UV laser operating at 25 Hz with a pulse duration of ~ 35 ns, which corresponds to a bandwidth of approximately 30 MHz. The main features of the laser system will be described elsewhere [32] and only the aspects relevant for the measurements of Rydberg spectra are emphasized here. The UV laser pulses at a wave number of $\sim 30\,700\text{ cm}^{-1}$ and with pulse energies of $\sim 200\ \mu\text{J}$ are generated by frequency-doubling in a β -barium-borate (BBO, BaB_2O_4) crystal (EK SMA Optics) of the pulse-amplified output of a pulsed-dye-amplification chain (Radiant Dyes, NarrowAmp) seeded by a linearly polarized single-mode continuous-wave ring dye laser (Coherent, Autoscan). The dye amplification medium, DCM in

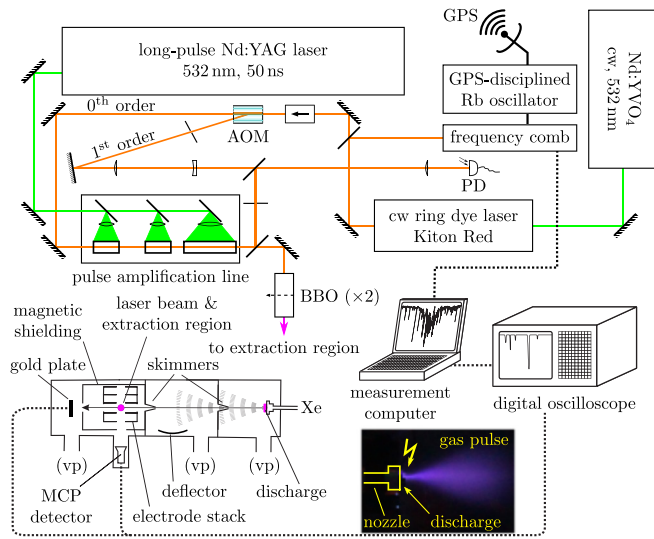


FIG. 2. Schematic representation of the experimental setup used to record high-resolution spectra of np and nf Rydberg series of Xe from the $(5p)^5(6s)^1\ ^3P_2$ metastable state. The upper part of the figure shows the laser system including calibration, pulse-amplification, and frequency up-conversion devices. The lower part displays the experimental vacuum chambers with supersonic beam, discharge source, photoexcitation, and detection regions. See text for details.

propylene carbonate, was pumped by the second harmonic of a home-built long-pulse Nd:YAG laser (30 mJ per pulse and pulse duration of 50 ns) [32]. This laser is inspired from Refs. [33–35] and consists of four diode-pumped Nd:YAG amplification stages (Northrop Grumman Cutting Edge Optonics, stage 1 & 2: RBAT34, stage 3: REA5006, stage 4: REA8006) amplifying seed laser pulses of 100 ns duration to pulse energies up to 680 mJ. The amplified radiation was frequency doubled in a 5-cm-long lithium-triborate crystal (Altechna), yielding 120 mJ per pulse at 532 nm. The input seed-laser pulses were chopped out of a linearly polarized continuous-wave fiber laser (IPG Photonics, YLR-1-1064-LP-SF) operating at a wavelength of 1064 nm using an amplitude modulator (JENOPTIK Optical Systems, AM1064b). The modulation signal was provided by an arbitrary-waveform generator (TABOR Electronics Ltd., WX2182B) allowing for a user-defined pulse shape and duration.

The laser frequency of the continuous-wave seed laser of the dye-amplification chain was calibrated by locking the ring dye laser to a frequency comb (Menlo Systems Inc., FC1500-250-WG), which was referenced to a GPS-disciplined Rb-atomic clock (Stanford Research Systems, model: FS725; GPS receiver: Scientific Instruments Inc, FS752) [36]. For this purpose, the beat-note signal formed between a tooth of the frequency comb and a small fraction of the ring dye laser output passed a home-built preamplifier and was compared with a quartz reference oscillator using a phase-frequency detector. The generated error signal was transferred through a PI controller and fed back to the ring-dye-laser control box modified as described in Ref. [37]. The comb-mode number contributing to the beat signal was unambiguously identified by measuring the

ring-laser frequency with a wavemeter (HighFinesse, WS7) specified to an accuracy of 20 MHz (1σ). The ring-dye-laser frequency was tuned by scanning the repetition rate of the frequency comb.

The offset and systematic uncertainty in the UV laser frequency caused by frequency shifts and chirps during pulse amplification were determined using a heterodyne beat-detection system [38,39]. The beat was formed between the seed-laser frequency ν_{seed} shifted by $\nu_{\text{AOM}} = +600$ MHz using an acousto-optic modulator (Brimrose, TEM-600-150) and a weak beam reflected off the fundamental output of the pulse-amplification chain. The single-shot beat profiles were detected using a fast photodiode (HAMAMATSU, S5973). The pulse envelope intensity $I_p(t)$, the phase evolution $\Phi(t)$, and the instantaneous frequency $\nu_{\text{inst}}(t)$ during the pulse were reconstructed in a Fourier analysis, as described in Ref. [39]. The instantaneous fundamental laser frequency can be expressed as

$$\nu_{\text{inst}} = \frac{1}{2\pi} \frac{d\Phi(t)}{dt} - \nu_{\text{AOM}} + \nu_{\text{seed}}. \quad (1)$$

The average frequency offset $\bar{\nu}_{\text{offset}}$ of the UV laser pulse from the doubled frequency of the seed laser was determined as a weighted average

$$\bar{\nu}_{\text{offset}} = \int 2\nu_{\text{inst}}(t)w(t)dt - 2\nu_{\text{seed}} \quad (2)$$

using

$$w(t) = \frac{I_p^2(t)}{\int I_p^2(t)dt} \quad (3)$$

as the weight function. Figure 3 displays the results of a representative measurement of the frequency chirp, adapted to include the effect of the second-harmonic generation using Eqs. (2) and (3). The frequency chirp turned out to be linear over the narrow frequency range of interest (see Fig. 5) and remained stable within 3 MHz over the entire period during which the spectra presented in Figs. 5–7 were measured.

The UV laser was directed into the high-vacuum chamber, where it crossed a doubly skimmed supersonic beam of metastable Xe at right angles on the axis of an electrode stack surrounding the photoexcitation region. The supersonic expansion was generated using a pulsed valve developed in the group of Leutwyler at the University of Bern [40]. Xe was excited to the $5p^56s[3/2]_2\ (^3P_2)$ metastable state near the valve orifice using a home-built dielectric-ring-barrier discharge induced by AC potentials of up to 3 kV. The two skimmers, with orifice diameters of 20 mm and 3 mm and located 10 cm and 45 cm downstream of the nozzle orifice, respectively, reduced the transverse velocity of the gas beam in the photoexcitation region. During operation of the pulsed valve, the background pressure in the photoexcitation region rose from about 10^{-7} mbar to 2×10^{-7} mbar.

The UV laser photoexcited the metastable Xe atoms to np and nf Rydberg states, which were pulse-field ionized ~ 300 ns after the laser pulse by an electric-field pulse of 410 V cm^{-1} applied using a high-potential switch (BEHLKE) across an impedance-matched cylindrically symmetric 7.8-cm-long stack of six equidistant and resistively coupled

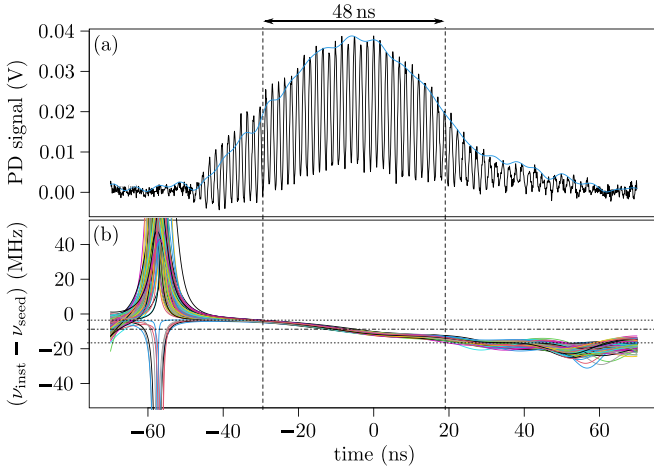


FIG. 3. Determination of the frequency chirp and shift resulting from the pulse amplification at a wave number of about $30\,731.7\text{ cm}^{-1}$. (a) Beat signal between the pulsed amplified radiation and the frequency-modulated cw output (black trace) and pulse envelope reconstructed from the DC-filtered data obtained by Fourier transform of the beat signal (blue trace). (b) Instantaneous frequency of the pulsed amplified radiation relative to the seed-laser frequency obtained by Fourier transform of the beat signal and filtering out the beat-note frequencies. The different traces show the results of multiple measurements carried out during the period over which the Rydberg spectra presented in this article were recorded. The dashed vertical and horizontal lines indicate the FWHM of the pulse temporal profile and the range over which the instantaneous frequency changed during the pulse, respectively. The dashed-dotted line indicates the weighted average of the frequency deviation from the seed-laser frequency.

parallel electrodes. The symmetry axis of the stack pointed in the direction perpendicular to both the gas and laser beams, and the electrode on the side of a microchannel-plate (MCP) detector was grounded. The xenon ions generated by pulsed-field ionization were extracted from the stack and accelerated towards the MCP detector located at the end of a short time-of-flight tube. The individual isotopes of Xe^+ could be well resolved in the ion time-of-flight spectrum and integration windows were set around their positions in the spectrum to record isotope-specific spectra. Rydberg spectra of all natural isotopes were recorded simultaneously and the integrated signal strengths were stored as a function of the laser frequency. The electrode stack and time-of-flight tube were surrounded by a double-layer mu-metal shield to reduce magnetic fields to below 5 mG.

III. EXPERIMENTAL RESULTS

A. General features of the spectra

Figure 4 presents an overview of the transitions to the nf and np Rydberg series in the range of principal quantum number $n \geq 55$ converging to the $^2P_{3/2}$ ground state of Xe^+ from the $(5p)^5(6s)^1\ ^3P_2$ metastable state of the seven most abundant natural isotopes of Xe. The spectra of the $I = 0$ nuclear-spin isotopes [^{128}Xe (1.910(13)%); ^{130}Xe (4.071(22)%); ^{132}Xe (26.909(55)%); ^{134}Xe (10.436(35)%); and ^{136}Xe (8.857(72)%)] are depicted in Fig. 4(a) and

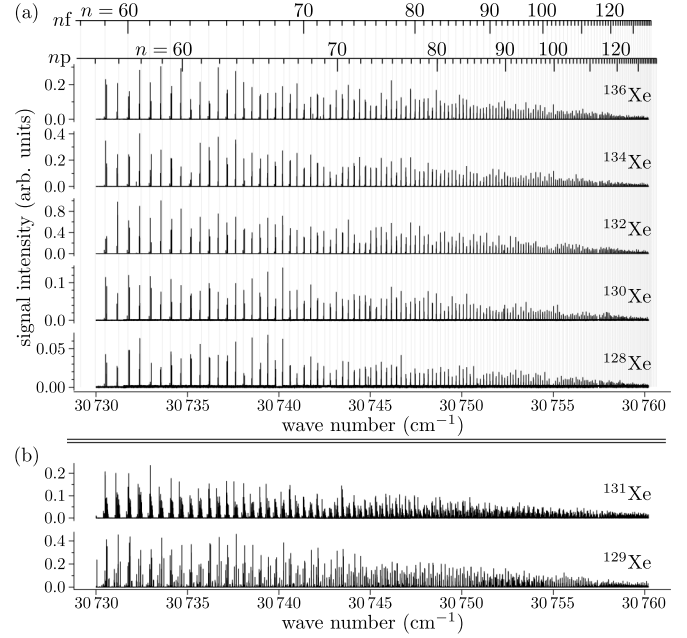


FIG. 4. Overview of the pulsed-field-ionization spectra of the np and nf Rydberg series of Xe converging on the $(5p)^5\ ^2P_{3/2}$ ground state of Xe^+ and recorded from the $(5p)^5(6s)^1\ ^3P_2$ metastable state. The spectra of the seven most abundant isotopes (indicated on the right of the figure) are displayed in separate panels with their intensity scale adapted so that all spectra have the same amplitude. The spectra of the $I = 0$ isotopes are displayed in (a) and those of the $I \neq 0$ isotopes in (b).

those of the isotopes with nonzero nuclear spins [^{129}Xe (26.401(138)%), $I = 1/2$) and ^{131}Xe (21.232(51)%), $I = 3/2$] in Fig. 4(b) [41]. For comparison, the range of intensities was adapted so that all spectra have approximately the same maximal amplitude. The spectra of the $I = 0$ isotopes consist of two distinct groups of lines corresponding to nf and $(n + 3)p$

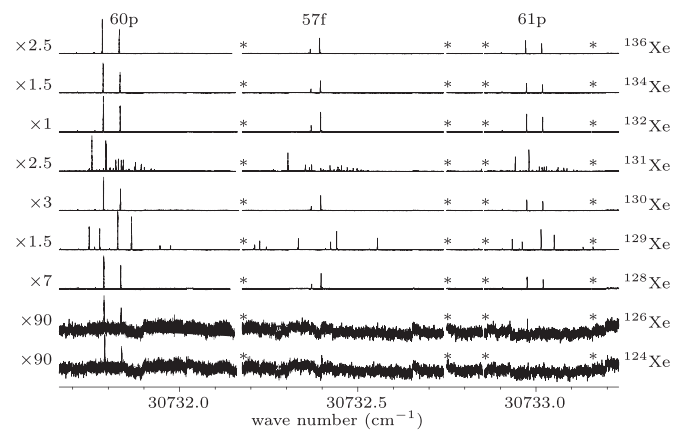


FIG. 5. Pulsed-field-ionization spectra of the $60p$, $57f$, and $61p$ Rydberg states of Xe belonging to series converging on the $(5p)^5\ ^2P_{3/2}$ ground state of Xe^+ and recorded from the $(5p)^5(6s)^1\ ^3P_2$ metastable state. The assignment of the fine and hyperfine structures of the spectra are provided in Figs. 6 and 7 and Tables I and II of the Supplemental Material [53]. The asterisks indicate small gaps in the spectrum caused by laser mode hops.

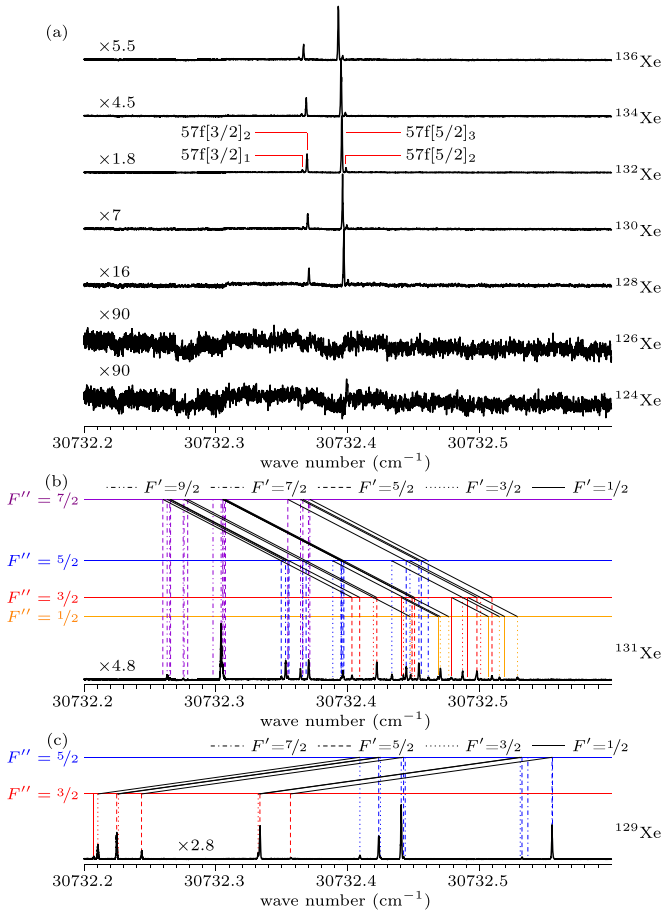


FIG. 6. Detailed view of the $(5p)^5 60p[k = 1/2, 3/2, 5/2]_{J=1,2,3} \leftarrow (5p)^5(6s)^1 {}^3P_2$ transitions of all natural isotopes of Xe. (a) Spectra of the $I = 0$ isotopes. (b) Spectrum of ^{131}Xe . (c) Spectrum of ^{129}Xe . In the case of the spectra of the $I \neq 0$ isotopes, the total-angular-momentum quantum numbers of the initial (F'') and final (F') states are encoded in the color of the assignment bar and in the line style, respectively. The diagonal black lines connect transitions with common final states. The asterisks indicate small gaps in the spectra caused by laser mode hops.

Rydberg states. Because the quantum defects of the f and p series differ by approximately 2.5 the members of the p series are located halfway between adjacent members of the f series. The np and nf series comprise several Rydberg series differing in the values of the k and J quantum numbers used in the Racah notation $n\ell^{(\prime)}[k]_J$ [6]. Although the series are displayed only up to $n = 140$, they are resolved up to about $n = 190$ [42].

The spectra of the $I \neq 0$ isotopes reveal a much more complex structure resulting from the hyperfine splittings of the initial and final states of the transitions. The 3P_2 metastable state of ^{129}Xe is split into two hyperfine components separated by an $F = 5/2 \rightarrow F = 3/2$ interval of 5961.2577(9) MHz, and that of ^{131}Xe consists of four hyperfine components with $F = 7/2 \rightarrow F = 5/2$, $F = 5/2 \rightarrow F = 3/2$ and $F = 3/2 \rightarrow F = 1/2$ intervals of 2693.6234(7), 1608.3475(8), and 838.7636(4) MHz, respectively [43]. As n increases, the hyperfine structure of the Rydberg states gradually evolves towards the hyperfine structure of the ${}^2P_{3/2}$ ion core, which

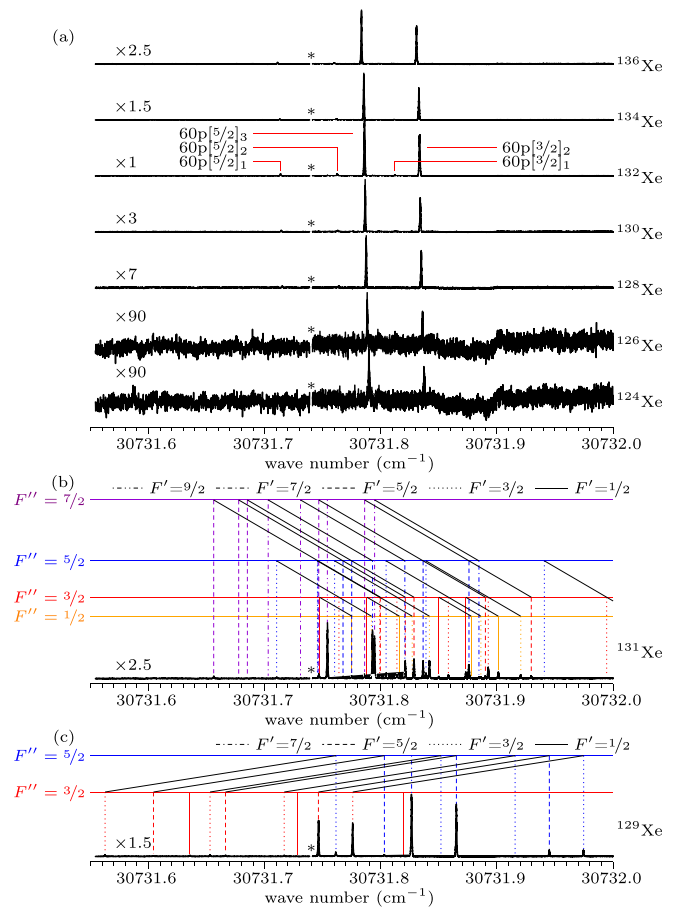


FIG. 7. Detailed view of the $(5p)^5 57f[k = 3/2, 5/2]_{J=1,2,3} \leftarrow (5p)^5(6s)^1 {}^3P_2$ transitions of the seven most abundant natural isotopes of Xe. (a) Spectra of the $I = 0$ isotopes. (b) Spectrum of ^{131}Xe . (c) Spectrum of ^{129}Xe . In the case of the spectra of the $I \neq 0$ isotopes, the total-angular-momentum quantum numbers of the initial (F'') and final (F') states are encoded in the color of the assignment bar and in the line style, respectively. The diagonal black lines connect transitions with common final states.

splits into a doublet with an $F^+ = 2 \rightarrow F^+ = 1$ interval of 1.64666(16) GHz in the case of $^{129}\text{Xe}^+$, and into four components spread over a range of about 1 GHz in the case of $^{131}\text{Xe}^+$ (see Table V below and Refs. [9,16]). The hyperfine structures of the different $n\ell[k]_J(F)$ series overlap spectrally and the series interact strongly at high n values, so that k and J are no longer good quantum numbers.

The fine and hyperfine structures of the series in the range of effective principal quantum number n^* around 60 are depicted on an enlarged scale in Fig. 5. The intensity distributions of the spectra of the $I = 0$ isotopes are dominated at each n value and for both the p and f series by only two transitions, to states with $k = 3/2, 5/2$ and $J = k + 1/2$. In the case of the $I \neq 0$ isotopes, the intensity is distributed over many more transitions, particularly in the case of ^{131}Xe , and the hyperfine structures of the p and f states almost overlap. Detailed views of the transitions to the $60p$ and $57f$ Rydberg states are presented with assignments in Figs. 6 and 7, respectively. The dynamic range of the intensities is very large, and the weakest lines are not visible on the scale of the figure. Their

measured positions are listed in the tables of the Supplemental Material [53]. The transitions to the $60p$ Rydberg levels are strong enough that the main lines could even be observed for the minor isotopes ^{124}Xe [natural abundance 0.095(5)%] and ^{126}Xe [0.089(3)%] [41]. At the enlarged horizontal scale of the figure, the isotope shifts of the transitions of the $I = 0$ isotopes start being visible and indicate a slight displacement of the lines to higher transition frequencies for decreasing mass number. These displacements are much smaller than the splittings caused by the hyperfine structure in the spectra of the $I \neq 0$ isotopes. The assignments of the transitions in terms of the quantum numbers k and J are ambiguous for these isotopes because the hyperfine interaction in the ion core, which does not change with n , becomes comparable in strength with the electrostatic interactions and gradually decouples \bar{l} from \bar{J}^+ at increasing n values. Consequently, in Fig. 5(b) the lines are only assigned in terms of the total-angular-momentum quantum numbers of the initial state (F'' , encoded through the color) and final state (F' , encoded through the line style). The spectra depicted in Figs. 6 and 7 illustrate the large increase in spectral complexity caused by the hyperfine structure, as was already noted in previous studies of Kr and Xe Rydberg states [9,15,28–30].

B. Transition frequencies and error budget

Table I lists the frequencies of all $60p/61p[k = 1/2, 3/2, 5/2]_{J=1,2,3}$ and $57f/58f[k = 3/2, 5/2]_{J=1,2,3} \leftarrow (5p)^5(6s)^1 \ ^3P_2$ transitions of the $I = 0$ isotopes of Xe that were measured with high accuracy using the frequency-comb-based calibration procedure. The corresponding frequencies of ^{129}Xe and ^{131}Xe are provided in the two tables of the Supplemental Material [53]. The uncertainties listed in these tables are purely statistical uncertainties (1σ) resulting from fits of Gaussian profiles to the individual lines. For intense, isolated lines, these uncertainties can be as small as $6 \times 10^{-6} \text{ cm}^{-1}$ (200 kHz), i.e., only $\approx 1/150$ of the full width at half maximum of ≈ 30 MHz.

The absolute accuracy of the frequency-comb-based calibration of the cw ring dye laser used as the seed laser for the pulse amplification is 10 kHz, determined by the accuracy of the GPS-disciplined Rb oscillator employed to determine the carrier-envelope-offset frequency and the repetition rate of the frequency comb. The analysis of the chirp measurements indicates a systematic shift of $-17.5(3.0)$ MHz of the UV laser frequency (see Sec. II).

In addition, systematic shifts and uncertainties from the DC- and AC-Stark effects, the first- and second-order Doppler effects, the photon recoil, as well as pressure shifts, were estimated, as summarized in Table II. The residual stray electric field in the measurement volume was determined to be 7.6 mV/cm [42]. No shifts could be detected for applied fields with strengths below 30 mV/cm. For the $(5p)^5(57f)[3/2]_2 \leftarrow (5p)^5(6s) \ ^3P_2$ transition, a frequency shift of $-10.5(2.0)$ MHz was measured for an applied field of 55 mV/cm, from which we estimated the Stark shift induced by the 7.6 mV/cm stray field to be $-200(40)$ kHz using the fact that the shifts scale with the square of the field. AC-Stark shifts were estimated by reducing the intensity of the UV laser. A reduction by a factor of 3 did not lead to a measurable shift.

Consequently, we estimate a contribution to the uncertainty of 200 kHz from the AC-Stark shift, corresponding to the precision with which we can determine the line centers from fits of the line profiles. Zeeman shifts are negligible because the double-layer magnetic shield reduces stray magnetic fields to below 5 mG in the photoexcitation region [36]. Pressure shifts are also negligible because the number densities of Xe in the doubly skimmed supersonic expansion are very low, of the order of 10^{12} cm^{-3} , at a distance of more than 60 cm from the nozzle orifice. The photon-recoil shift [given by $h\nu^2/(2mc^2)$] is only 14.3 kHz in the frequency range of interest because of the large mass of Xe. The second-order Doppler shift [given by $-\nu v^2/(2c^2)$] is negligible at the current precision because of the slow average velocity (305 m/s) of the supersonic beam.

The main contribution to the systematic uncertainty is from a possible residual first-order Doppler shift originating from a deviation from 90° of the angle between the supersonic and laser beams. To minimize this shift and estimate the systematic uncertainty, we measured transition frequencies after retroreflection of the UV laser beam and assessing the overlap of the forward- and backward-propagating laser beams at a distance of 40 cm from the reflection mirror. To record the spectra of both beams separately, we introduced a small reflection angle in the plane perpendicular to the supersonic beam thus generating ions in two separate regions along the direction parallel to the axis of the time-of-flight mass spectrometer. Because of the different distances from the two distinct ion clouds to the MCP detector, the corresponding ions were detected in different temporal windows of the time-of-flight spectra and integrated separately. The results of such measurements are presented in Fig. 8, where the full black line corresponds to the spectrum recorded with the forward-propagating beam and the spectra drawn in color correspond to spectra recorded with the reflected beam. The spectrum drawn in red was obtained when both beams crossed the supersonic beam at right angles. The other spectra were measured for slight displacements of -2 mm (cyan), 3 mm (orange), and 4.5 mm (blue), corresponding to reflection angles of $180^\circ + \alpha$, with $\alpha = -0.29^\circ, 0.43^\circ$, and 0.64° , respectively, and first-order Doppler shifts $\Delta\nu_{\text{Doppler}}^{\text{shift}} = \nu v/(c \sin \alpha)$ of -4.7 MHz, 7.0 MHz, and 10.5 MHz at the transition frequencies. A lateral displacement of 3 mm of the forward- from the backward-propagating beam is detectable. Consequently, we take a conservative value of 7 MHz for the systematic uncertainty originating from the first-order Doppler effect in our measurements.

Table II reveals that the measured frequencies have to be corrected by -17.31 MHz and that their systematic uncertainty is 10.3 MHz ($3.44 \times 10^{-4} \text{ cm}^{-1}$). The transition frequencies listed in Table I include the -17.31 MHz frequency correction ($-5.774 \times 10^{-4} \text{ cm}^{-1}$) resulting from this analysis. The systematic uncertainties of these measurements determine the uncertainties of the absolute ionization energies of Xe, as explained in the next section. They do not affect the isotopic shifts as strongly because these were measured simultaneously, i.e., under the same experimental conditions, so that the systematic errors largely cancel out. We estimate that the isotopic shifts have systematic uncertainties of less than 3 MHz.

TABLE I. Wave numbers of the transitions from the $(5p)^5(6s)^1\ ^3P_2$ metastable state of the $I = 0$ isotopes of Xe to $60p/61p/57f/58f[k = 1/2, 3/2, 5/2]_{J=1,2,3}$ Rydberg states below the $^2P_{3/2}$ ground state of Xe^+ . The transitions are grouped by isotope. For each isotope, the first column lists the measured transition wave numbers (after subtraction of 30730 cm^{-1}) with their statistical uncertainties (1σ), the second column the binding energies $E_b = hc\tilde{\nu}_b$ calculated by MQDT, and the third column the deviation of ionization energy of the metastable state, obtained as a sum of the transition energy and the binding energy, from the fitted value of this quantity. The fitted ionization energies are provided in a separate line at the bottom of the respective line list. All values are given in cm^{-1} .

Final state	$\tilde{\nu}_{\text{exp}}$	$\tilde{\nu}_b$	$\frac{\Delta E_I}{10^{-6}hc}$	$\tilde{\nu}_{\text{exp}}$	$\tilde{\nu}_b$	$\frac{\Delta E_I}{10^{-6}hc}$	$\tilde{\nu}_{\text{exp}}$	$\tilde{\nu}_b$	$\frac{\Delta E_I}{10^{-6}hc}$
^{132}Xe									
60p[1/2] ₁	1.71372(7)	34.496418	−54	1.71312(14)	34.496420	−67	1.71100(15)	34.496422	−134
60p[5/2] ₂	1.76249(7)	34.447690	−17	1.76192(13)	34.447692	5	1.75988(14)	34.447694	11
60p[5/2] ₃	1.785973(6)	34.424228	5	1.785397(7)	34.424230	18	1.783338(8)	34.424232	11
60p[3/2] ₁	1.81213(18)	34.398081	12	1.8114(5)	34.398083	−173			
60p[3/2] ₂	1.833432(7)	34.376730	−34	1.832833(10)	34.376732	−44	1.830754(22)	34.376734	−71
57f[3/2] ₁	2.36564(7)	33.844575	16	2.36502(15)	33.844577	−9	2.36296(18)	33.844579	−20
57f[3/2] ₂	2.369135(18)	33.841083	22	2.36854(3)	33.841085	19	2.36646(3)	33.841087	−10
57f[5/2] ₃	2.395557(14)	33.814686	47	2.394953(21)	33.814688	32	2.392893(19)	33.814690	24
57f[5/2] ₂	2.39874(5)	33.811484	32	2.39818(9)	33.811486	59	2.39608(12)	33.811488	52
61p[1/2] ₁	2.9052(4)	33.304959	−81	2.90452(6)	33.304961	−125	2.90253(6)	33.304963	−63
61p[5/2] ₂	2.95146(12)	33.258732	−2	2.95092(21)	33.258734	48			
61p[5/2] ₃	2.973769(10)	33.236460	34	2.973173(16)	33.236462	26	2.971103(16)	33.236464	8
61p[3/2] ₂	3.018798(11)	33.191397	0	3.018203(15)	33.191399	−7	3.016122(19)	33.191401	−35
58f[3/2] ₁	3.5237(4)	32.686437	−46	3.5230(5)	32.686439	−188			
58f[3/2] ₂	3.52712(7)	32.683119	43	3.52657(10)	32.683121	85	3.52447(12)	32.683123	37
58f[5/2] ₃	3.552061(23)	32.658066	−68	3.55142(16)	32.658068	−121	3.54925(4)	32.658070	−206
58f[5/2] ₂	3.55503(22)	32.655025	−137	3.5544(3)	32.655027	−139			
	30766.210195(8)			30766.209609(9)			30766.207559(10)		
^{130}Xe									
60p[1/2] ₁	1.71429(16)	34.496415	−35	1.71515(22)	34.496413	−31			
60p[5/2] ₂	1.76306(16)	34.447687	−63	1.76398(15)	34.447685	141			
60p[5/2] ₃	1.786546(10)	34.424225	6	1.787418(18)	34.424223	79	1.78980(4)	34.424218	13
60p[3/2] ₂	1.834031(13)	34.376728	−12	1.834772(12)	34.376725	−68	1.83730(6)	34.376721	5
57f[3/2] ₁	2.3663(3)	33.844573	23						
57f[3/2] ₂	2.36970(4)	33.841081	11	2.37055(12)	33.841078	35			
57f[5/2] ₃	2.39611(3)	33.814684	24	2.39699(3)	33.814681	108	2.39928(8)	33.814677	−50
57f[5/2] ₂	2.39933(16)	33.811481	32	2.4002(5)	33.811479	135			
61p[1/2] ₁	2.90576(9)	33.304957	−63	2.9065(5)	33.304955	−89			
61p[5/2] ₂	2.9521(6)	33.258730	80						
61p[5/2] ₃	2.974338(22)	33.236458	18	2.97521(5)	33.236456	92			
61p[3/2] ₂	3.019354(24)	33.191395	−25	3.02024(6)	33.191393	59	3.02260(11)	33.191388	−17
58f[3/2] ₂	3.52764(15)	32.683117	−13	3.52860(15)	32.683115	151			
58f[5/2] ₃	3.55260(4)	32.658064	−146						
	30766.210773(8)			30766.21157(3)			30766.21401(3)		
^{126}Xe									
60p[5/2] ₃	1.78834(7)	34.424221	0						
60p[3/2] ₂	1.8359(7)	34.376723	42						
	30766.21256(7) ^a								

^aUncertainty dominated by a single transition frequency.

IV. MQDT ANALYSIS AND DETERMINATION OF THE IONIZATION ENERGIES

To determine the ionization energies, MQDT calculations of the binding energies of the $60p/61p/57f/58f[k = 3/2, 5/2]_{J=1,2,3}$ states were performed using the parameters determined in a previous investigation of the high np and nf Rydberg states of Xe by millimeter-wave spectroscopy [9]. These parameters include quantum defects and their

energy dependence for the relevant close-coupling channels, as described below. Separate calculation procedures were followed for the $I = 0$ isotopes and $I \neq 0$ isotopes, although in both cases the same close-coupling quantum-defect parameters were used, based on the (excellent) approximation that the hyperfine interaction is much weaker than all other interactions (electrostatic interactions including exchange interaction, spin-orbit interactions) in the close-coupling region of the electron–ion–core collision complex [28]. The

TABLE II. Error budget for the determination of the frequencies of the $(60p)/(61p)/(57f)/(58f) \leftarrow (5p)^5(6s)^1 \ ^3P_2$ transitions of Xe. See text for details.

	Correction	Uncertainty
Frequency chirp	−17.5 MHz	3 MHz
DC-Stark shift ^a	+200 kHz	≲ 40 kHz
AC-Stark shift		≲ 200 kHz
Zeeman shift		≲ 10 kHz
Pressure shift		1 kHz
First-order Doppler shift		7 MHz
Second-order Doppler shift	+0.63 kHz	≪ 1 kHz
Photon-recoil shift	−14.3 kHz	
Systematic uncertainty		10.3 MHz
Frequency correction	−17.31 MHz	

^aFor the $(5p)^5(57f)[3/2]_2 \leftarrow (5p)^5(6s)^1 \ ^3P_2$ transition.

calculations for the $I = 0$ isotopes were based on the MQDT formalism first employed by Lu [20] and Lee and Lu [21] in their analyses of the absorption spectra of argon and xenon. The calculations for ^{129}Xe relied on the extension of their formalism to include the effect of the hyperfine interaction in the dissociation channels, as introduced for the analysis of VUV-laser spectra of the ns and nd Rydberg series [28] of ^{83}Kr following an earlier similar treatment outlined by Sun [27]. This extended MQDT formalism was used and refined in the analyses of the np series of ^3He [44], the $n\ell$ ($\ell = s, p, d$, and f) Rydberg series of ^{83}Kr [30] and ^{129}Xe and ^{131}Xe [9], the ns and nd series of ^{165}Ho [45], and of the ns series of ^{171}Yb [46]. Particularly relevant for the present study was the global MQDT fit of the np and nf series of Xe by Schäfer *et al.* [9], which included a very broad range of earlier experimental data in addition to the very precise set of millimeter-wave transition frequencies connecting high Rydberg states of the s, p, d , and f series also reported in Ref. [9]. The MQDT parameters determined in this global fit turned out to describe the relative positions of all levels of the isotopes observed in the present investigation within their experimental uncertainties. Consequently, only the ionization energies of the metastable Xe isotopes needed to be adjusted to reach perfect agreement

TABLE III. Natural isotopes of Xe (^AXe) with nuclear-spin quantum number I_A , natural abundance h_A [41], isotopic mass m_A [47], and ionization energy $E_{I,A}$ with respect to the $(5p)^5(6s)^1 \ (^3P_2)$ metastable state.

A	I_A	$h_A/\%$	m_A/u	$\frac{E_{I,A}}{hc} / \text{cm}^{-1\text{a}}$
124	0	0.095(5)	123.9058852(15)	30 766.21401(3)
126	0	0.089(3)	125.904297422(6)	30 766.21256(7)
128	0	1.910(13)	127.903530753(6)	30 766.21157(3)
129	1/2	26.401(138)	128.904780857(5)	30 766.212370(7) ^b
130	0	4.071(22)	129.903509347(10)	30 766.210773(8)
131	3/2	21.232(51)	130.905084128(5)	30 766.212233(4) ^b
132	0	26.909(55)	131.904155083(5)	30 766.210195(8)
134	0	10.436(35)	133.905393030(6)	30 766.209609(9)
136	0	8.857(72)	135.907214474(7)	30 766.207559(10)

^aThis work.

^bCenter of gravity.

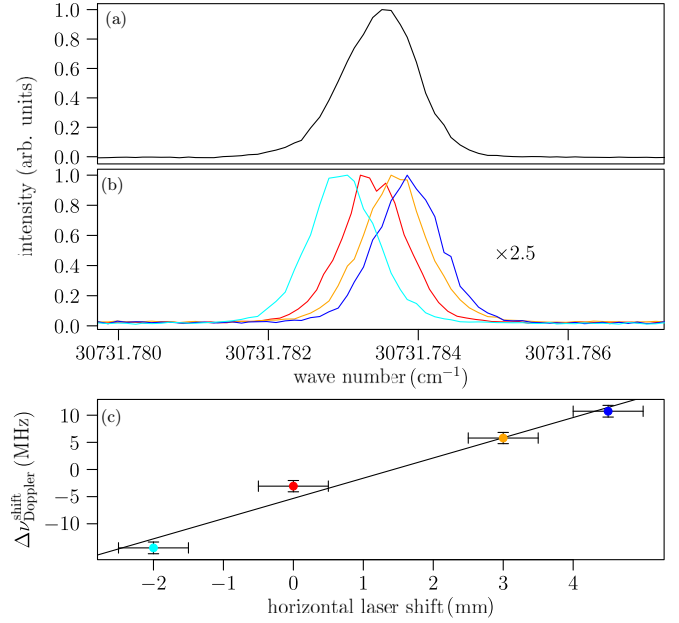


FIG. 8. Determination of the uncertainty in the transition frequencies originating from the first-order Doppler shift from spectra recorded in a retroreflection arrangement of the UV laser beam. (a) Spectrum recorded with the forward-propagating beam. (b) Spectra recorded with the retroreflected beam after optimizing the overlap of the forward and backward propagating laser beams at a distance of 40 cm from the mirror (red trace) and introducing intentional displacements of the photoexcitation spots of −2 mm (cyan), 0 mm, 3 mm (orange), and 4.5 mm (blue) along the time-of-flight mass spectrometer. (c) Doppler shifts as a function of the displacement. See text for details.

with the experimental data presented in Figs. 5–7. In the following subsections, we briefly summarize the procedure followed in the calculations.

A. p and f Rydberg series of the $I = 0$ isotopes of Xe

To determine the ionization energies of the $I = 0$ isotopes of Xe, we calculated the binding energies of the $60p/61p/57f/58f[k = 3/2, 5/2]_{J=1,2,3}$ states and added them to the observed transition frequencies. In this way, every observed line enabled an independent determination of the ionization energy. In the calculations, we used the formalism of Lu [20] and Lee and Lu [21] with the MQDT parameters derived by Schäfer *et al.* [9]. In the following, the main equations are recapitulated using the same notation as in Ref. [9]. The calculations rely on an angular-momentum frame transformation between the close-coupling region of the electron–ion–core collision, which is described by LS coupling

$$\vec{L}^+ + \vec{\ell} = \vec{L}, \quad \vec{S}^+ + \vec{s} = \vec{S}, \quad \vec{L} + \vec{S} = \vec{J}, \quad (4)$$

and the long-range region, which follows J^+j coupling according to

$$\vec{L}^+ + \vec{S}^+ = \vec{J}^+, \quad \vec{\ell} + \vec{s} = \vec{j}, \quad \vec{J}^+ + \vec{j} = \vec{J}. \quad (5)$$

The binding energy E of the Rydberg levels is defined with respect to the $E(^2P_{3/2})$ ground state using the effective principal

quantum numbers $\nu_{3/2}$ and $\nu_{1/2}$ defined by

$$E = -\frac{hcR_M}{(\nu_{3/2})^2} = E(^2P_{1/2}) - \frac{hcR_M}{(\nu_{1/2})^2}, \quad (6)$$

where $R_M = R_\infty \frac{M^+}{M}$ is the mass-corrected Rydberg constant determined from the atomic and ion-core masses M and $M^+ = M - m_e$, respectively, and $E(^2P_{1/2})$ is the energy of the upper spin-orbit level [$E(^2P_{1/2})/(hc) = 10\,536.925(19)$ cm⁻¹ in Xe [29]].

The binding energies with respect to the two ionization limits are defined according to Eq. (6). They correspond to the nontrivial solutions of the equation

$$\sum_{\alpha} U_{i\alpha} \sin[\pi(\nu_i + \mu_{\alpha})] A_{\alpha} = 0, \quad (7)$$

and satisfy the condition

$$\det |U_{i\alpha} \sin[\pi(\nu_i + \mu_{\alpha})]| = 0, \quad (8)$$

where A_{α} is the expansion coefficient of the radial part of the Rydberg-electron wave function in the basis of the close-coupling eigenchannels α . $U_{i\alpha}$ are the elements of an $N \times N$ transformation matrix

$$U_{i\alpha} = \sum_{\bar{\alpha}} U_{i\bar{\alpha}} V_{\bar{\alpha}\alpha}, \quad (9)$$

which is a product of the pure angular-momentum frame transformation $U_{i\bar{\alpha}} = \langle LSJ | J^+ j J \rangle$ connecting the $J^+ j$ and LS bases and a matrix with elements $V_{\bar{\alpha}\alpha}$ which accounts for the deviations from pure LS coupling of the close-coupling channels. In the formalism of Lee and Lu [21], the $V_{\bar{\alpha}\alpha}$ elements are described by products of rotation matrices $\mathbf{R}(\theta_{jk})$ involving channel-mixing angles θ_{jk} according to

$$V_{\bar{\alpha}\alpha} = \prod_j \prod_{k>j} \mathbf{R}(\theta_{jk}) = \mathbf{R}(\theta_{12})\mathbf{R}(\theta_{13}) \dots \mathbf{R}(\theta_{23}) \dots \quad (10)$$

In Eq. (10), $\mathbf{R}(\theta_{jk})$ are defined as

$$R_{mm}(\theta_{jk}) = \begin{cases} \cos \theta_{jk} & \text{if } m = j \text{ or } m = k, \\ 1 & \text{otherwise,} \end{cases}$$

$$R_{mn}(\theta_{jk}) = \begin{cases} -\sin \theta_{jk} & \text{if } m = j, n = k \\ \sin \theta_{jk} & \text{if } m = k, n = j \\ 0 & \text{otherwise} \end{cases} m \neq n. \quad (11)$$

The energy dependence of the close-coupling quantum defects μ_{α} is weak and can be described in good approximation by linear functions of the energy $\epsilon = -(\nu_{3/2})^{-2}$ according to

$$\mu_{\alpha} = \mu_{\alpha}^0 + \epsilon \mu_{\alpha}^1. \quad (12)$$

The quantum defects parameters μ_{α}^0 and μ_{α}^1 , the mixing angles θ_{jk} and the transformation matrix elements $U_{i\alpha}$ listed in Table VII of Ref. [9] were found to describe all observed relative transition frequencies in the spectra of all $I = 0$ isotopes within the experimental uncertainties. Consequently, it was sufficient to only fit the ionization energy of the metastable state to reach a quantitatively fully satisfactory description of the observed transition frequencies. The third and sixth columns of Table I list the binding energies $E_b = hc\tilde{\nu}_b$ of the observed np and nf levels. The sums of these binding

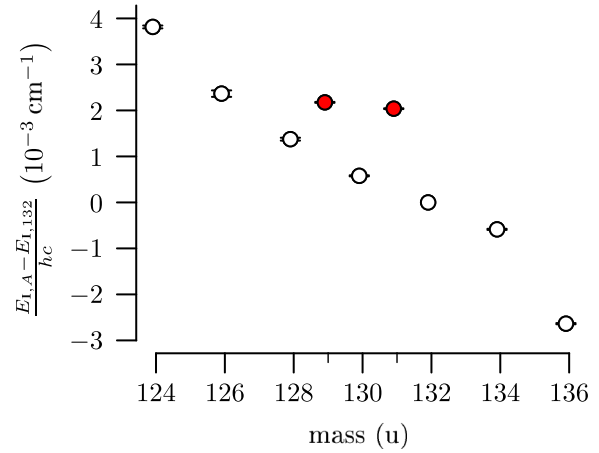


FIG. 9. Isotopic shifts of the ionization energies of the $(5p)^5(6s)^1 \ ^3P_2$ metastable states of the isotopes of Xe determined from the spectra of transitions to the $60p$, $61p$, $57f$, and $58f$ Rydberg states and MQDT calculations of the binding energies using the quantum-defect parameters reported by Schäfer *et al.* [9]. The red data points are the centroids (i.e., hyperfine-free) ionization energies of ^{129}Xe and ^{131}Xe .

energies and the corresponding observed transition frequencies represent the ionization energy of the $(5p)^5(6s)^1 \ ^3P_2$ state of Xe. The fourth, seventh, and tenth columns of the table give, for each $I = 0$ isotope, the differences between the ionization energies obtained from the individual transition frequencies from the fitted values of the ionization energies. The fitted values of the ionization energies of the different isotopes and their statistical uncertainties are provided below the respective line lists in Table I. The uncertainties range from 8×10^{-6} cm⁻¹ (0.24 MHz) for ^{132}Xe to 7×10^{-5} cm⁻¹ (2.1 MHz) for ^{126}Xe , a value which is almost entirely determined by the statistical uncertainty of the only line that could be determined accurately for this rare natural isotope.

Figure 9 displays the ionization energies of the metastable state of the $I = 0$ isotopes of Xe as a function of their mass number as open circles with error bars. The mass-dependent isotopic shifts clearly deviate from the linear behavior typically observed for light nuclei and expected from the normal and specific mass shifts. In heavy nuclei, field shifts can become observable (see, e.g., Refs. [48–50]), especially when the transition frequencies or energy intervals are observed for a broad range of isotopes, as in the present case.

B. p and f Rydberg series of ^{129}Xe and ^{131}Xe

For the calculation of the Rydberg states of the $I \neq 0$ isotopes of Xe, we followed the procedure introduced for the analysis of the ns and nd Rydberg series of ^{83}Kr converging to the $^2P_{3/2}$ ground state of Kr^+ [28]. This procedure consists in neglecting the effects of the nuclear spins on the close-coupling quantum defects μ_{α} and mixing angles θ_{jk} while considering their effects on the dissociation channels through the hyperfine-structure of the ion core. The rationale for this procedure follows from the extreme weakness of the hyperfine interaction compared to the other interactions (spin-orbit

and electrostatic interactions) in the close-coupling region. In contrast, in high Rydberg states the hyperfine splittings of the ion core become comparable to, and even larger than, the interactions involving the Rydberg electron because these scale as n^{-3} . They can be even larger than the energetic separation between states of neighboring quantum numbers because these also scale as n^{-3} (see Figs. 4 and 5).

In this (extremely good) approximation, the effect of the hyperfine interaction can be treated using exactly the same MQDT parameters as for the $I = 0$ isotopes, but by extending the angular momentum frame transformation from an $LS \leftrightarrow J^+ j$ transformation $U_{i\bar{\alpha}} = \langle LSJ|J^+ jJ \rangle$ to an $LSJF \leftrightarrow J^+ F^+ jF$ frame transformation $U_{i_f \bar{\alpha}_F} = \langle LSJF|J^+ F^+ jF \rangle$ given by [9,28,30]

$$\begin{aligned} \langle LSJF|J^+ F^+ jF \rangle &= (2F+1)\sqrt{(2J+1)(2L+1)(2S+1)(2j+1)(2F^++1)(2J^++1)} \\ &\times \sum_{m_j, m_{j^+}, m_J, m_\ell, m_{L^+}, m_L, m_s, m_{S^+}, m_S, m_{F^+}, m_I} (-1)^{F^+-j-J^++2I-J+L-S-2s+3m_F+m_{j^+}+2m_J} \\ &\times \begin{pmatrix} I & J & F \\ m_I & m_J & -m_F \end{pmatrix} \begin{pmatrix} L & S & J \\ m_L & m_S & -m_J \end{pmatrix} \begin{pmatrix} L^+ & \ell & L \\ m_{L^+} & m_\ell & -m_L \end{pmatrix} \begin{pmatrix} S^+ & s & S \\ m_{S^+} & m_s & -m_S \end{pmatrix} \\ &\times \begin{pmatrix} F^+ & j & F \\ m_{F^+} & m_j & -m_F \end{pmatrix} \begin{pmatrix} \ell & s & j \\ m_\ell & m_s & -m_j \end{pmatrix} \begin{pmatrix} I & J^+ & F^+ \\ m_I & m_{J^+} & -m_{F^+} \end{pmatrix} \begin{pmatrix} L^+ & S^+ & J^+ \\ m_{L^+} & m_{S^+} & -m_{J^+} \end{pmatrix} \quad (13) \end{aligned}$$

for any chosen value of m_F . Simultaneously, the binding energies must be defined with respect to the positions of the ionization thresholds $E_{I_F} \equiv E(^2P_{J^+F^+})$ corresponding to the four (for ^{129}Xe) or six (for ^{131}Xe) hyperfine levels of the ion, according to

$$E = E(^2P_{J^+F^+}) - \frac{hcR_M}{(v_{J^+F^+})^2}. \quad (14)$$

In the same way as the ionization energy of the $I = 0$ isotopes can be fitted to match the observed line positions, both the ionization energy and the ionic hyperfine splittings can be fitted for the $I \neq 0$ isotopes, and this was used in previous work to determine the hyperfine structures of both the $^2P_{3/2}$ and $^2P_{1/2}$ spin-orbit components of the Xe^+ ground state [9,29].

The quantum-defect parameters derived in Ref. [9] could be used without adjustments to reproduce the experimental relative line positions within their uncertainties. Only the ionization energies of ^{129}Xe and ^{131}Xe and the hyperfine-structure splitting of the $^2P_{3/2}$ ground state of $^{129}\text{Xe}^+$ and $^{131}\text{Xe}^+$ were adjusted in the least-squares fit. In ^{129}Xe , both the 3P_2 metastable state and $^2P_{3/2}$ ground ionic state are split

into a doublet by the hyperfine interaction. In the fit, we kept the hyperfine splittings of the 3P_2 metastable state to the values determined in Ref. [43] and adjusted, for each isotope, the hyperfine coupling constants of the ion (A^+ for $^{129}\text{Xe}^+$ and A^+ and B^+ for $^{131}\text{Xe}^+$) as well as the ‘‘hyperfine-free’’ or center-of-gravity (c.o.g.) ionization energies, i.e., the energy difference between the centers of gravity of the $\text{Xe}^+ ^2P_{3/2}$ hyperfine levels and the $\text{Xe} ^3P_2$ hyperfine levels.

The results of this analysis are presented in Table V which lists the c.o.g. ionization energies and hyperfine-coupling constants of the $^2P_{3/2}$ ground state of $^{129}\text{Xe}^+$ and $^{131}\text{Xe}^+$. The table also contains the term values of the hyperfine levels of $^{129}\text{Xe}^+$ with respect to the $F = 5/2$ hyperfine level of the 3P_2 level of ^{129}Xe , and those of $^{131}\text{Xe}^+$ with respect to the $F = 7/2$ hyperfine level of the 3P_2 level of ^{131}Xe . Tables VI and VII give the term values of the observed levels of ^{129}Xe

TABLE IV. Term values of the $(5p)^5(6s)^1 (^3P_2)$ metastable state of all natural Xe isotopes determined using the ionization energies of this state listed in Table III and the isotopic shifts of the ionization energy from the ground state reported in Ref. [31].

A	T'_A/cm^{-1}
124	67 067.547(11)
126	67 067.557(11)
128	67 067.565(11)
129	67 067.565(11) ^a
130	67 067.573(11)
131	67 067.571(11) ^a
132	67 067.580(11)
134	67 067.586(11)
136	67 067.597(11)

^aCenter of gravity.

TABLE V. Results of the least-squares fit of the center-of-gravity (hyperfine-free) ionization energy with respect to the center-of-gravity energy level of the 3P_2 metastable state of ^{129}Xe and ^{131}Xe , respectively, and of the hyperfine constants A^+ and B^+ for the ground state of $^{129}\text{Xe}^+$ and $^{131}\text{Xe}^+$ based on MQDT calculations using parameters reported in Ref. [9]. The energy levels E_{I_F} of the hyperfine levels of $^{129}\text{Xe}^+$ and $^{131}\text{Xe}^+$ with respect to the center-of-gravity term value of the 3P_2 metastable state of ^{129}Xe and ^{131}Xe derived from these values are given in the bottom part of the table.

Fitted values	^{129}Xe	^{131}Xe
$E_1(\text{c.o.g.})/(hc \text{ cm}^{-1})$	30 766.212370(7)	30 766.212233(4)
A^+/cm^{-1}	-0.054929(7)	0.0162898(22)
B^+/cm^{-1}		0.008669(10)
Degrees of freedom	47	111
Weighted rms	3.7521	1.8843
Derived values:		
$E_{13}/(hc \text{ cm}^{-1})$		30 766.251051(7)
$E_{12}/(hc \text{ cm}^{-1})$	30 766.171173(8)	30 766.193512(9)
$E_{11}/(hc \text{ cm}^{-1})$	30 766.281031(11)	30 766.169602(8)
$E_{10}/(hc \text{ cm}^{-1})$		30 766.161982(16)

TABLE VI. Term values T' of ^{129}Xe relative to the metastable $(5p)^5(6s)^1\ ^3P_2$, $F = 5/2$ state. The letters in parentheses serve as labels to link the corresponding observed transitions of Table A in the Supplemental Material [53] to the corresponding term in this table.

$n\ell$	F	T'/cm^{-1}	$n\ell$	F	T'/cm^{-1}	$n\ell$	F	T'/cm^{-1}
$6s\ (^3P_2)$	5/2	0.0 (exact)	$57f\ (c)$	5/2	30 732.423548(8)	$61p\ (f)$	3/2	30 733.03847(4)
$6s\ (^3P_2)$	3/2	0.19885000(11)	$57f\ (d)$	3/2	30 732.42493(10)	$61p\ (g)$	5/2	30 733.051097(11)
$60p\ (a)$	3/2	30 731.761369(18)	$57f\ (e)$	7/2	30 732.440600(11)	$61p\ (h)$	3/2	30 733.10418(24)
$60p\ (b)$	5/2	30 731.80306(4)	$57f\ (f)$	5/2	30 732.442507(17)	$61p\ (i)$	3/2	30 733.10425(6)
$60p\ (c)$	7/2	30 731.826499(5)	$57f\ (g)$	3/2	30 732.53089(7)	$61p\ (j)$	5/2	30 733.132277(13)
$60p\ (d)$	1/2	30 731.83453(5)	$57f\ (h)$	5/2	30 732.532282(19)	$61p\ (k)$	3/2	30 733.160256(16)
$60p\ (e)$	3/2	30 731.85180(4)	$57f\ (i)$	7/2	30 732.555095(12)	$58f\ (a)$	3/2	30 733.56724(6)
$60p\ (f)$	5/2	30 731.865074(5)	$57f\ (j)$	5/2	30 732.55575(17)	$58f\ (b)$	5/2	30 733.58083(4)
$60p\ (g)$	3/2	30 731.91566(4)	$61p\ (a)$	3/2	30 732.95273(5)	$58f\ (c)$	7/2	30 733.597018(23)
$60p\ (h)$	5/2	30 731.945187(4)	$61p\ (b)$	5/2	30 732.99199(9)	$58f\ (d)$	5/2	30 733.59886(16)
$60p\ (i)$	3/2	30 731.974628(5)	$61p\ (c)$	5/2	30 732.99211(20)	$58f\ (e)$	3/2	30 733.6882(3)
$57f\ (a)$	1/2	30 732.40616(4)	$61p\ (d)$	7/2	30 733.014290(9)	$58f\ (f)$	5/2	30 733.68947(4)
$57f\ (b)$	3/2	30 732.409256(12)	$61p\ (e)$	1/2	30 733.02486(6)			

and ^{131}Xe . The transition frequencies and the deviation from the fitted term values are listed in Tables A and B of the Supplemental Material [53]. The MQDT-fit residuals for the observed transitions in ^{129}Xe and ^{131}Xe are shown in Figs. 1 and 2 of the Supplemental Material [53], respectively. In most cases, the residuals are smaller than the experimental uncertainties. The weighted root-mean-square deviation of the fits of the transition frequencies of ^{129}Xe and ^{131}Xe are 3.8 and 1.9. The c.o.g. ionization energies of ^{129}Xe and ^{131}Xe are plotted as red circles in Fig. 9.

The value of $A_{3/2}^+ = -0.054\,955(15)\text{cm}^{-1}$ for ^{129}Xe lies close to the value of $A_{3/2}^+ = -0.054\,9265(52)\text{cm}^{-1}$ determined from millimeter-wave transitions between high Rydberg states in Ref. [9], and is approximately halfway between the values of -0.06118cm^{-1} and -0.04587cm^{-1} recently advocated by Blondel and Drag from an analysis of the angular pattern in the hyperfine structure of Xe I [26]. The values of $A_{3/2}^+ = 0.016\,2898(22)\text{cm}^{-1}$ and $B_{3/2}^+ = 0.008\,669(10)\text{cm}^{-1}$ for ^{131}Xe are also in very good agreement with the values of $A_{3/2}^+ = 0.016\,2829(21)\text{cm}^{-1}$ and

TABLE VII. Term values T' of ^{131}Xe relative to the metastable $(5p)^5(6s)^1\ ^3P_2$, $F = 1/2$ state. The letters in parentheses serve as labels to link the corresponding observed transitions of Table B in the Supplemental Material [53] to the corresponding term in this table.

$n\ell$	F	T'/cm^{-1}	$n\ell$	F	T'/cm^{-1}	$n\ell$	F	T'/cm^{-1}
$6s\ (^3P_2)$	1/2	0.0 (exact)	$57f\ (d)$	7/2	30 732.43709(10)	$61p\ (c)$	3/2	30 733.0168(9)
$6s\ (^3P_2)$	3/2	0.0279770(3)	$57f\ (e)$	9/2	30 732.44731(11)	$61p\ (d)$	5/2	30 733.01886(7)
$6s\ (^3P_2)$	5/2	0.0816260(5)	$57f\ (f)$	3/2	30 732.44825(6)	$61p\ (e)$	3/2	30 733.030262(17)
$6s\ (^3P_2)$	7/2	0.1714750(6)	$57f\ (g)$	5/2	30 732.450641(17)	$61p\ (f)$	5/2	30 733.037907(19)
$60p\ (a)$	3/2	30 731.79253(7)	$57f\ (h)$	1/2	30 732.46911(11)	$61p\ (g)$	5/2	30 733.045705(24)
$60p\ (b)$	1/2	30 731.8166(6)	$57f\ (i)$	3/2	30 732.470943(25)	$61p\ (h)$	1/2	30 733.06482(14)
$60p\ (c)$	3/2	30 731.8278(3)	$57f\ (j)$	3/2	30 732.47115(23)	$61p\ (i)$	3/2	30 733.07287(7)
$60p\ (d)$	5/2	30 731.82824(4)	$57f\ (k)$	9/2	30 732.475951(8)	$61p\ (j)$	1/2	30 733.08739(3)
$60p\ (e)$	3/2	30 731.842489(16)	$57f\ (l)$	7/2	30 732.47713(3)	$61p\ (k)$	7/2	30 733.0917(6)
$60p\ (f)$	5/2	30 731.849617(18)	$57f\ (m)$	5/2	30 732.47734(25)	$61p\ (l)$	5/2	30 733.105183(21)
$60p\ (g)$	5/2	30 731.857147(14)	$57f\ (n)$	7/2	30 732.47858(6)	$61p\ (m)$	3/2	30 733.106615(23)
$60p\ (h)$	7/2	30 731.875109(7)	$57f\ (o)$	7/2	30 732.47862(13)	$61p\ (n)$	9/2	30 733.113832(10)
$60p\ (i)$	1/2	30 731.87851(5)	$57f\ (p)$	5/2	30 732.4796(4)	$61p\ (o)$	5/2	30 733.144089(17)
$60p\ (j)$	3/2	30 731.886797(23)	$57f\ (q)$	1/2	30 732.50726(15)	$61p\ (p)$	7/2	30 733.15213(23)
$60p\ (k)$	1/2	30 731.901766(11)	$57f\ (r)$	3/2	30 732.51572(3)	$61p\ (q)$	7/2	30 733.152373(7)
$60p\ (l)$	7/2	30 731.90281(19)	$57f\ (s)$	1/2	30 732.5198(5)	$58f\ (a)$	3/2	30 733.2049(3)
$60p\ (m)$	5/2	30 731.918684(12)	$57f\ (t)$	5/2	30 732.526645(22)	$58f\ (b)$	5/2	30 733.58952(21)
$60p\ (n)$	3/2	30 731.921096(9)	$57f\ (u)$	3/2	30 732.52949(7)	$58f\ (c)$	7/2	30 733.59261(23)
$60p\ (o)$	9/2	30 731.926091(5)	$57f\ (v)$	7/2	30 732.53620(4)	$58f\ (d)$	5/2	30 733.60777(6)
$60p\ (p)$	5/2	30 731.958081(7)	$57f\ (w)$	7/2	30 732.536231(17)	$58f\ (e)$	9/2	30 733.63246(4)
$60p\ (q)$	7/2	30 731.96665(8)	$57f\ (x)$	5/2	30 732.53806(5)	$58f\ (f)$	7/2	30 733.63354(18)
$60p\ (r)$	7/2	30 731.966706(7)	$57f\ (y)$	7/2	30 732.54341(12)	$58f\ (g)$	7/2	30 733.63498(22)
$57f\ (a)$	5/2	30 732.43182(8)	$61p\ (a)$	1/2	30 732.9672(3)	$58f\ (h)$	3/2	30 733.67318(12)
$57f\ (b)$	7/2	30 732.43510(3)	$61p\ (b)$	3/2	30 732.98368(12)	$58f\ (i)$	7/2	30 733.69266(8)
$57f\ (c)$	7/2	30 732.43512(3)						

$B_{3/2}^+ = 0.008\,6887(82)\text{ cm}^{-1}$ reported in Ref. [9]. The ionization energies of ^{129}Xe and ^{131}Xe deviate from the trend in the shifts of the other isotopes. Deviation of isotopic shifts in transition frequencies of isotopes having odd mass numbers are not uncommon and have been observed before for other transitions of Xe [31].

The average value of the ionization energy of all nine isotopes, weighted by their natural abundance gives an ionization energy $E_I(\text{Xe}^+ \ ^2P_{3/2} \leftarrow \text{Xe}^* \ ^3P_2)/(hc) = 30\,766.2110(3)\text{ cm}^{-1}$, which lies ≈ 1 GHz below the value of $31\,766.240(11)\text{ cm}^{-1}$ one obtains from the recommended values of the ionization energy of ground-state Xe $E_I(\text{Xe}^+ \ ^2P_{3/2} \leftarrow \text{Xe} \ ^1S_0)/(hc) = 97\,833.787(11)\text{ cm}^{-1}$ [1,31] and the recommended term value of $67\,067.547\text{ cm}^{-1}$ for the $(5p)^5(6s)^1 \ ^3P_2$ metastable state [1,16]. The present results thus suggest an overall correction of all tabulated term values of the electronically excited states of Xe by -0.0303 cm^{-1} . Term values of the 3P_2 metastable state for all nine natural abundant Xe isotopes are listed in Table IV which were deduced from the ionization energies of this state reported here (see Table III) and the isotopic shift of the ionization energy from the ground state reported in Ref. [31].

V. CONCLUSION

This article presented a measurement of the np and nf Rydberg series of Xe from the $(5p)^5(6s)^1 \ ^3P_2$ metastable state

using a narrow-band tunable UV laser. An MQDT analysis of these spectra enabled the determination of accurate values of the ionization energies of all nine natural isotopes of Xe, of precise isotopic shifts, and of the hyperfine splitting in the $^2P_{3/2}$ ground state of $^{129}\text{Xe}^+$ and of $^{131}\text{Xe}^+$. Through a careful assessment and reduction of multiple sources of systematic uncertainties, the transition frequencies and ionization energies could be determined with an overall uncertainty of only 12 MHz, dominated by the contribution from the Doppler shift arising from a possible deviation from 90° of the crossing angle of the laser and supersonic beams. In the future, this uncertainty could be reduced by a better control of the retroreflection angle of the laser beam, for example, by using an interferometric procedure [51,52]. The accuracy of the ionization energies of only 12 MHz demonstrated here is two orders of magnitude better than what could be achieved using the new technique of PRFI-ZEKE photoelectron spectroscopy [42]. The ionization energy of Xe was found to be ≈ 1 GHz lower than previous literature values, suggesting that the term values of the electronically excited states of Xe [1] should all be corrected by this amount.

ACKNOWLEDGMENTS

We thank Hansjürg Schmutz and Josef A. Agner for technical support. This work was supported financially by the Swiss National Science Foundation (Grant No. 200020B-200478).

-
- [1] A. Kramida, Y. Ralchenko, J. Reader, and NIST ASD Team, NIST atomic spectra database (2018).
- [2] H. Saßmannshausen, F. Merkt, and J. Deiglmayr, High-resolution spectroscopy of Rydberg states in an ultracold cesium gas, *Phys. Rev. A* **87**, 032519 (2013).
- [3] J. Deiglmayr, H. Herburger, H. Saßmannshausen, P. Jansen, H. Schmutz, and F. Merkt, Precision measurement of the ionization energy of Cs I, *Phys. Rev. A* **93**, 013424 (2016).
- [4] M. Peper, F. Helmrich, J. Butscher, J. A. Agner, H. Schmutz, F. Merkt, and J. Deiglmayr, Precision measurement of the ionization energy and quantum defects of ^{39}K I, *Phys. Rev. A* **100**, 012501 (2019).
- [5] M. Mack, F. Karlewski, H. Hattermann, S. Höckh, F. Jessen, D. Cano, and J. Fortágh, Measurement of absolute transition frequencies of ^{87}Rb to nS and nD Rydberg states by means of electromagnetically induced transparency, *Phys. Rev. A* **83**, 052515 (2011).
- [6] G. Racah, On a new type of vector coupling in complex spectra, *Phys. Rev.* **61**, 537 (1942).
- [7] C. E. Moore, *Atomic Energy Levels*, NBS Circular 467, Vol. III (National Bureau of Standards, Washington, DC, 1958).
- [8] J. E. Sansonetti and W. C. Martin, Handbook of basic atomic spectroscopic data, *J. Phys. Chem. Ref. Data* **34**, 1559 (2005).
- [9] M. Schäfer, M. Raunhardt, and F. Merkt, Millimeter-wave spectroscopy and multichannel quantum-defect-theory analysis of high Rydberg states of xenon: The hyperfine structure of $^{129}\text{Xe}^+$ and $^{131}\text{Xe}^+$, *Phys. Rev. A* **81**, 032514 (2010).
- [10] H. Beutler, Über Absorptionsserien von Argon, Krypton und Xenon zu Termen zwischen den beiden Ionisierungsgrenzen $^2P_{3/2}^o$ und $^2P_{1/2}^o$, *Z. Phys.* **93**, 177 (1935).
- [11] K. Yoshino, Absorption spectrum of the argon atom in the vacuum-ultraviolet region, *J. Opt. Soc. Am.* **60**, 1220 (1970).
- [12] K. Yoshino and D. E. Freeman, Absorption spectrum of xenon in the vacuum-ultraviolet region, *J. Opt. Soc. Am. B* **2**, 1268 (1985).
- [13] K. Maeda, K. Ueda, and K. Ito, High-resolution measurement for photoabsorption cross sections in the autoionization regions of Ar, Kr and Xe, *J. Phys. B: At. Mol. Opt. Phys.* **26**, 1541 (1993).
- [14] I. D. Petrov, V. L. Sukhorukov, and H. Hotop, Autoionizing Rydberg series $n_c p_{1/2}^5 n \ell' [K']_J (\ell' = 0 - 5)$ of Ne, Ar, Kr, and Xe: General trends for the resonance widths, *J. Phys. B: At. Mol. Opt. Phys.* **35**, 323 (2002).
- [15] Th. A. Paul, J. Liu, and F. Merkt, Nuclear spin effects in the photoionization of krypton, *Phys. Rev. A* **79**, 022505 (2009).
- [16] V. L. Sukhorukov, I. D. Petrov, M. Schäfer, F. Merkt, M.-W. Ruf, and H. Hotop, Photoionization dynamics of excited Ne, Ar, Kr and Xe atoms near threshold, *J. Phys. B: At. Mol. Opt. Phys.* **45**, 092001 (2012).
- [17] U. Fano, Sullo spettro di assorbimento dei gas nobili presso il limite dello spettro d'arco, *Nuovo Cim.* **12**, 154 (1935).
- [18] U. Fano, Effects of configuration interaction on intensities and phase shifts, *Phys. Rev.* **124**, 1866 (1961).
- [19] U. Fano, Interaction between configurations with several open shells, *Phys. Rev.* **140**, A67 (1965).
- [20] K. T. Lu, Spectroscopy and collision theory. The Xe absorption spectrum, *Phys. Rev. A* **4**, 579 (1971).
- [21] C.-M. Lee and K. T. Lu, Spectroscopy and collision theory. II. the Ar absorption spectrum, *Phys. Rev. A* **8**, 1241 (1973).

- [22] U. Fano, Unified treatment of perturbed series, continuous spectra and collisions, *J. Opt. Soc. Am.* **65**, 979 (1975).
- [23] M. J. Seaton, Quantum defect theory, *Rep. Prog. Phys.* **46**, 167 (1983).
- [24] M. Kono, Y. He, K. G. H. Baldwin, and B. J. Orr, Sub-Doppler two-photon spectroscopy of 33 Rydberg levels in atomic xenon excited at 205–213 nm: Diverse isotopic and hyperfine structure, *J. Phys. B: At. Mol. Opt. Phys.* **46**, 035401 (2013).
- [25] M. Kono, Y. He, K. G. H. Baldwin, and B. J. Orr, Sub-Doppler two-photon-excitation Rydberg spectroscopy of atomic xenon: Mass-selective studies of isotopic and hyperfine structure, *J. Phys. B: At. Mol. Opt. Phys.* **49**, 065002 (2016).
- [26] C. Blondel and C. Drag, The angular pattern in the hyperfine structure of Xe I and Kr I atoms, *J. Phys. B: At. Mol. Opt. Phys.* **55**, 015001 (2022).
- [27] J.-Q. Sun, Multichannel quantum defect theory of the hyperfine structure of high Rydberg states, *Phys. Rev. A* **40**, 7355 (1989).
- [28] H. J. Wörner, U. Hollenstein, and F. Merkt, Multichannel quantum defect theory of the hyperfine structure of high Rydberg states of ^{83}Kr , *Phys. Rev. A* **68**, 032510 (2003).
- [29] H. J. Wörner, M. Grütter, E. Vliegen, and F. Merkt, Role of nuclear spin in photoionization: Hyperfine-resolved photoionization of Xe and multichannel quantum defect theory analysis, *Phys. Rev. A* **71**, 052504 (2005); **73**, 059904(E) (2006).
- [30] M. Schäfer and F. Merkt, Millimeter-wave spectroscopy and multichannel quantum-defect-theory analysis of high Rydberg states of krypton: The hyperfine structure of $^{83}\text{Kr}^+$, *Phys. Rev. A* **74**, 062506 (2006).
- [31] F. Brandi, I. Velchev, W. Hogervorst, and W. Ubachs, Vacuum-ultraviolet spectroscopy of Xe: Hyperfine splittings, isotope shifts, and isotope-dependent ionization energies, *Phys. Rev. A* **64**, 032505 (2001).
- [32] H. Herburger, J. A. Agner, H. Schmutz, U. Hollenstein, and F. Merkt (unpublished).
- [33] A. Gerakis, M. N. Shneider, and B. C. Stratton, Remote-sensing gas measurements with coherent Rayleigh-Brillouin scattering, *Appl. Phys. Lett.* **109**, 031112 (2016).
- [34] A. Gerakis, M. N. Shneider, Y. Raitses, and B. C. Stratton, Electrostrictive in-situ nanoparticle detection with coherent Rayleigh-Brillouin scattering (Conference Presentation), in *Optical Trapping and Optical Micromanipulation XIV*, edited by K. Dholakia and G. C. Spalding, International Society for Optics and Photonics (SPIE, Bellingham, WA, 2017), Vol. 10347, p. 103470J.
- [35] A. Gerakis, Controlling and probing molecular motion with optical lattices, Ph.D. Thesis, University College London, London, United Kingdom (2014).
- [36] N. Hölsch, M. Beyer, E. J. Salumbides, K. S. E. Eikema, W. Ubachs, C. Jungen, and F. Merkt, Benchmarking theory with an improved measurement of the ionization and dissociation energies of H_2 , *Phys. Rev. Lett.* **122**, 103002 (2019).
- [37] D. Haubrich and R. Wynands, A modified commercial Ti:sapphire laser with 4 kHz rms linewidth, *Opt. Commun.* **123**, 558 (1996).
- [38] M. S. Fee, K. Danzmann, and S. Chu, Optical heterodyne measurement of pulsed lasers: Toward high-precision pulsed spectroscopy, *Phys. Rev. A* **45**, 4911 (1992).
- [39] S. Gangopadhyay, N. Melikechi, and E. E. Eyler, Optical phase perturbations in nanosecond pulsed amplification and second-harmonic generation, *J. Opt. Soc. Am. B* **11**, 231 (1994).
- [40] Designed by S. Leutwyler and H. M. Frey, Constructed by the Mechanical and Electronic workshops of the Department of Chemistry and Biochemistry, Freiestrasse 3, Universität Bern, CH-3012 Bern, Switzerland (2014).
- [41] J. Meija, T. B. Coplen, M. Berglund, W. A. Brand, P. De Bièvre, M. Gröning, N. E. Holden, J. Irrgeher, R. D. Loss, T. Walczyk, and T. Prohaska, Isotopic compositions of the elements 2013 (IUPAC Technical Report), *Pure Appl. Chem.* **88**, 293 (2016).
- [42] H. Herburger, V. Wirth, U. Hollenstein, and F. Merkt, Pulsed-ramped-field-ionisation zero-kinetic-energy photoelectron spectroscopy of the metastable rare-gas atoms Ar, Kr and Xe, *Phys. Chem. Chem. Phys.* **25**, 22437 (2023).
- [43] W. L. Faust and M. N. McDermott, Hyperfine structure of the $(5p)^5(6s)^3P_2$ state of ^{129}Xe and ^{131}Xe , *Phys. Rev.* **123**, 198 (1961).
- [44] W. Hogervorst, E. A. J. M. Bente, R. J. de Graaff, C. T. W. Lahaije, and W. Vassen, Laser spectroscopy of bound and autoionizing Rydberg series of two-electron atoms, *Phys. Scr.* **1989**, 9 (1989).
- [45] F. Robicheaux, D. W. Booth, and M. Saffman, Theory of long-range interactions for Rydberg states attached to hyperfine-split cores, *Phys. Rev. A* **97**, 022508 (2018).
- [46] N. Chen, L. Li, W. Huie, M. Zhao, I. Vetter, C. H. Greene, and J. P. Covey, Analyzing the Rydberg-based optical-metastable-ground architecture for ^{171}Yb nuclear spins, *Phys. Rev. A* **105**, 052438 (2022).
- [47] M. Wang, W. Huang, F. Kondev, G. Audi, and S. Naimi, The AME 2020 atomic mass evaluation (II). Tables, graphs and references, *Chin. Phys. C* **45**, 030003 (2021).
- [48] W. H. King, The estimation of mass shifts in optical isotope shifts, *J. Phys. B: At. Mol. Phys.* **4**, 288 (1971).
- [49] W. H. King, *Isotope Shifts in Atomic Spectra* (Plenum, New York, 1984).
- [50] P. Aufmuth, K. Heilig, and A. Steudel, Changes in mean-square nuclear charge radii from optical isotope shifts, *At. Data Nucl. Data Tables* **37**, 455 (1987).
- [51] S. Hannemann, E. J. Salumbides, and W. Ubachs, Reducing the first-order Doppler shift in a Sagnac interferometer, *Opt. Lett.* **32**, 1381 (2007).
- [52] H. Müller, S.-W. Chiow, Q. Long, C. Vo, and S. Chu, Active sub-Rayleigh alignment of parallel or antiparallel laser beams, *Opt. Lett.* **30**, 3323 (2005).
- [53] See Supplemental Material at <http://link.aps.org/supplemental/10.1103/PhysRevA.109.032816> for a list of all observed transitions from the $(5p)^5(6s)^{13}P_2$ metastable state to the 60p, 57f, 61p and 58f Rydberg states of ^{129}Xe and ^{131}Xe and of the MQDT-fit residuals of the transition frequencies.